# On the propagation of the effect of targeted observations: The 2000 Winter Storm Reconnaissance Program

Istvan Szunyogh[1]

*UCAR Visiting Scientist at NCEP, Camp Springs, Maryland, USA;*

Zoltan Toth,

*SAIC at NCEP, Camp Springs, Maryland, USA*

Aleksey V. Zimin,

*Department of Physics, University of Maryland, College Park, Maryland, USA*

Sharanya J. Majumdar, and

*Department of Meteorology, The Pennsylvania State University, University Park, Pennsylvania, USA*

Anders Persson

*European Centre for Medium Range Weather Forecasts, Shinfield Park, Reading, UK*

October 9, 2001

---

[1] *Corresponding author:* Institute for Physical Science and Technology, University of Maryland, Computer and Space Sciences Building, College Park, MD, 20742-2431, E-mail:szunyogh@ipst.umd.edu

# Abstract

The propagation of the effect of targeted observations in numerical weather forecasts is investigated, based on results from the 2000 Winter Storm Reconnaissance (WSR00) program. In this field program, nearly 300 dropsondes were released adaptively at selected locations over the northeast Pacific on 12 separate flight days with the aim of reducing the risk of major failures in severe winter storm forecasts over the United States. The data impact was assessed by analysis-forecast experiments carried out with the T62 horizontal resolution, 28-level version of the operational global Medium Range Forecasting system of the National Centers for Environmental Prediction.

In some cases, storms that reached the west-coast or Alaska were observed in an earlier phase of their development, while at other times the goal was to improve the prediction of storms that formed far downstream of the targeted region. Changes in the forecasts were the largest when land-falling systems were targeted and the baroclinic energy conversion was strong in the targeted region.

As expected from the experience accumulated during the 1999 Winter Storm Reconnaissance (WSR99) program, downstream baroclinic development played a major role in propagating the influence of the targeted data over North-America. The results also show, however, that predicting the location of significant changes due to the targeted data in the forecasts can be difficult in the presence of a nonzonal large scale flow. The strong zonal variations in the large scale flow over the northeast Pacific during WSR00 did not reduce the positive forecast effects of the targeted data. On the contrary, the overall impact of the dropsonde data was more positive than during WSR99, when the large scale flow was dominantly zonal on the flight days. This can be attributed to the improved prediction of the large scale flow that led to additional improvements in the prediction of the synoptic scale waves.

# 1 Introduction

Reducing the risk of a major forecast failure in the prediction of a weather event with potentially large societal impact is the primary motivation for *targeting* weather observations. The data targeting procedure involves three time levels: In the first step, a potentially severe weather event is selected at *planning* time $t_p$ based on the latest forecast products. A *future verification time* ($t_v$) and a *verification region* for the event are chosen accordingly. A *sensitivity analysis* is then carried out to determine the *future observational time* ($t_o$; $t_p < t_o < t_v$) and *observational* region from where extra observations taken at $t_o$ are most likely to significantly reduce the error in the prediction of the selected weather event at $t_v$.

Recently, the concept of targeting has been tested by idealized model experiments (Emanuel et al. 1996, Lorenz and Emanuel 1998, Morss et al. 2000a, b) and by deploying dropsonde observations from aircraft in Northern Hemisphere winter field programs (e.g. Snyder 1996, Langland et al. 1999, Szunyogh et al. 1999a,b,2000, Toth et al. 2000, 2001). The main differences between the targeting strategies proposed by the different research teams are related to the sensitivity analysis algorithms. Some of these algorithms are based on integrating *tangent-linear equations* (e.g. Bergot et al. 1999, Montani et al. 1999, Gelaro et al. 1999, Pu and Kalnay 1999, Pu et al. 1998) while others, such as the Ensemble Transform (Bishop and Toth 1999, Szunyogh et al. 1999a) and the Ensemble Transform Kalman Filter (Bishop et al. 2001, Majumdar et al. 2001a,b) techniques, are based on investigating the time evolution of an ensemble of nonlinear model forecasts. The common element of these methods is that they are all *linear inferences* applied to a set of numerical forecasts assuming that linear processes play an important role in propagating the effect of targeted observations.

Objective targeting techniques proved to have skill in adaptively selecting an observational region: changes in the initial conditions within the observational region at $t_o$ typically led to considerable changes in the forecast in the verification region at $t_v$. Moreover, dropsonde data, especially those collected over the northeast Pacific, on average had positive effects both on the forecast of the selected weather event and in general. This assessment is true for all analysis-forecast systems evaluated so far although the extent of the forecast error reduction is system dependent (Langland et al. 1999).

While the evaluation studies have so far provided convincing empirical evidence that targeting observations is an operationally attainable way to improve forecasts, the exact dynamical/synoptical mechanisms through which targeted observations realize their beneficial forecast effects have not yet been fully explored. Our first attempt to gain a better understanding of the dynamical processes that govern the propagation of the effect of targeted observations was documented in Szunyogh et al. (2000, SEA). The major findings of SEA, based on data from the 1999 Winter Storm Reconnaissance Program (WSR99), were:

- The Ensemble Transform (ET) and Ensemble Transform Kalman Filter (ETKF) techniques pointed to the upstream section of baroclinic wave developments over the northeast Pacific as the optimal observational region for improving the prediction of intense winter storms over the continental United States including Alaska. For the Alaskan and some west-coast verification regions, the land-falling storm in its earlier stage was sampled by the targeted data. The impact of the dropsonde data was expected to propagate at a speed faster then the synoptic systems in the remaining west-coast and all east-coast storm cases.

- For forecast lead times longer than 12-24 hours, the surface pressure signal, defined by the magnitude of the difference between surface pressure forecasts with and without the assimilation of the dropsonde data at observation time, propagated eastward at an average speed of $30^o$ per day. Local maxima in the surface pressure signal occurred where the leading edge of the signal reached regions of strong baroclinicity, while the surface impact was moderate in areas of weak baroclinicity. Storms that belonged to the second group above were all located at the *leading edge* of the eastward propagating surface pressure signal.
- On average, surface pressure errors were reduced by 10-20% at the leading edge of the signal. That is, regularly observing the eastward propagating synoptic waves over the northeast Pacific improved the prediction of mid-latitude storms along the Pacific and the Atlantic storm tracks, even *beyond the life span of the individual systems* observed.

SEA argued that these results strongly indicated that over the United States the effect of the targeted dropsonde observations propagated like upper tropospheric wave packets generated by baroclinic energy conversion. It is important to recall, however, that the large scale flow was predominantly zonal on flight days when the extra observations led to indisputable forecast error reduction in WSR99. Studies investigating idealized flow regimes found that downstream propagating baroclinic waves can gain or lose a substantial amount of kinetic energy in regions of strong zonal inhomogenities (e.g. Bishop 1993a,b, Whitaker and Dole 1995). This means that in the general case, when the waves may lose energy, the potential for forecast improvement may also be reduced due to the weakened influence of the upstream flow on the evolution of flow in a downstream region.

Data collected during the 2000 Winter Reconnaissance Program (WSR00) provide an excellent opportunity to test the robustness of the targeting results to changes in the large-scale flow. During this field program, the large-scale flow was highly non-zonal in the northeast Pacific, and the main region of baroclinic energy conversion was out of reach for targeting by the available aircraft. The main goal of this paper is to explore how the propagation of the effect of targeted dropsonde observations is modified by the presence of strong zonal variations in the large scale atmospheric flow. This research was motivated by the finding, also presented here, that targeted data had even more positive overall effect on forecast quality in WSR00 than in WSR99.

The outline of the paper is as follows. An overview of the relationship between large-scale atmospheric dispersion processes, leading edge dynamics, downstream baroclinic development and signal propagation is given in section 2. Section 3 describes the WSR00 program and the analysis-forecast system that was used to evaluate the effect of targeted data. In section 4, an analysis of the flow regimes is presented, while section 5 describes the results of the analysis-forecast experiments in detail. Section 6 gives an assessment of the impact of targeted data on forecast quality while section 7 offers some conclusions.

# 2 Background

## 2.1 Linear models of signal propagation

The underlying dynamical problem of targeting is not new in Numerical Weather Prediction (NWP). It was first raised by Ertel (1941 and 1944) and later by Rossby (1949) and Charney (1949) shortly before the discipline of NWP was born. With Charney's words: *"The concept of the speed of propagation of a hydro-dynamical influence, or "signal velocity", in the atmosphere is an important one for meteorology. It is used to determine the dimension of the region through which the initial data are needed in forecasting for a prescribed area, and more generally, it enters in any investigation of the causal connection between part of the atmosphere and another."*

The early authors assumed that the state vector $\mathbf{x}(0)$ representing the atmospheric flow at an initial time can be expressed as the sum of a basic flow $\overline{\mathbf{x}}(0)$ and a superposition of small amplitude wave components $\mathbf{x}'(0)$), i.e.

$$\mathbf{x}(0) = \overline{\mathbf{x}}(0) + \mathbf{x}'(0)\,. \tag{1}$$

If the nonlinear evolution of $\mathbf{x}(t)$ is determined by

$$\mathbf{x}(t) = \mathbf{f}(\mathbf{x}(0)), \tag{2}$$

the time evolution of an arbitrary perturbation (signal) $\mathbf{s}(t)$ is then given by

$$\mathbf{s}(t) = \mathbf{f}(\overline{\mathbf{x}}(0) + \mathbf{x}'(0) + \mathbf{s}(0)) - \mathbf{x}(t)\,. \tag{3}$$

Hence, the nonlinear evolution of the signal is determined by complex interactions between the signal, waves and basic flow.

When the amplitude of the wave component is small a linear model can explain its evolution reasonably well, i.e.

$$\mathbf{x}'(t) = \mathbf{L}(\overline{\mathbf{x}})\mathbf{x}'(0)\,. \tag{4}$$

Since the signal magnitude is typically not larger than the wave amplitude, the same linear model can also well approximate the evolution of the signal:

$$\mathbf{s}(t) = \mathbf{L}(\overline{\mathbf{x}})\mathbf{s}(0). \tag{5}$$

The time evolution of the initially localized small perturbation, $\mathbf{s}(t)$ is determined by the superposition of the evolving wave components that satisfies the initial condition $\mathbf{s}(0)$. After an initial transient period, changes in the flow become negligible at locations whose distance from the initial disturbance is larger than $t \mid \mathbf{C}_{gr} \mid_{max}$ (Charney 1949, Pedlosky 1987, Phillips 1990). Here,

$| \mathbf{C}_{gr} |_{max}$ is the magnitude of the largest possible group velocity in the linear model defined by Eq. 4.

For dispersive waves, the propagation velocity of a hydro-dynamical influence (group velocity) and the velocity of the individual wave crests (phase velocity) are different in both magnitude and direction (Pedlosky 1987). The largest group velocity depends both on the choice of the linearized equation, $\mathbf{L}$, and the basic flow, $\overline{\mathbf{x}}$. By examining the dispersion relation for Rossby waves on a stationary zonal flow, the early authors (Rossby 1945,1949, Yeh 1949) deduced an important rule: Since there is always a range of wave lengths of atmospheric waves for which the eastward component of the group velocity exceeds their eastward phase speed, *errors in the analysis of an atmospheric disturbance have degrading effects, not only on the prediction of the evolution of the wave itself, but also on the waves that develop further downstream.*

Early estimates of the signal and group velocities were based on the linearized barotropic vorticity equation. On the other hand, severe winter storms owe their existence to baroclinic energy conversion processes in the atmosphere. Phillips (1976) made the first attempt to obtain a quantitative estimate of the forecast degradation over land due to the propagation of analysis errors from oceanic regions by *unstable baroclinic waves.* Using a linearized two-layer quasi-geostrophic model to simulate the propagation of the impact of hypothetical satellite observations over the Pacific, he demonstrated that significant contributions to the forecast error over the North American continent arose due to poor data coverage over the ocean.

## 2.2 Nonlinear models of signal propagation

The time evolution of the dropsonde signal (described in the introduction) is, in several respects, reminiscent of the nonlinear spatio-temporal evolution of an initially small-amplitude and *zonally localized* disturbance described by Swanson and Pierrehumbert (1994). These authors demonstrated that *linear theory* correctly described the *dynamics of the leading edge* of the nonlinearly evolving wave packet. They also showed that the evolution of the main body of the wave packet behind the leading edge was highly nonlinear.

What the results of Swanson and Pierrehumbert (1994) cannot explain is our observation that local maxima in the surface pressure signal occurred where the leading edge of the signal reached regions of strong baroclinicity, while the surface impact was moderate in areas of weak baroclinicity. This phenomenon can be understood by acknowledging that in the real atmosphere (and in a state-of-the-art forecast model), the baroclinicity of the atmospheric layers is not constant as was assumed by Swanson and Pierrehumbert (1994). Instead, strong maxima of baroclinicity exist at the upstream fringe of storm tracks. The conceptual model of storm tracks, proposed by Chang and Orlanski (1993), takes these inhomogenities into account. In their model, the central role is played by *downstream baroclinic development*: eddy kinetic energy is generated in a localized region of baroclinic energy conversion and then transported eastward by the upper tropospheric flow. (The speed of this transport is on average

$30^o$/day at a latitude of $45^o$N, Persson 2000) The signature of the eastward propagating waves at the surface is weak in regions of weak low-level baroclinicity. In areas of strong low-level baroclinicity, however, the Lagrangian transport of the eddy kinetic energy can contribute to the kinetic energy of a new deep baroclinic development either (1) directly or (2) by first generating potential energy through the divergence of ageostrophic geopotential fluxes (Orlanski and Katzfey 1991, Persson 2000). This means that the leading edge of the atmospheric wave packet is not only the farthest location where the hydrodynamical influence can travel from the origin of the wave packet, but also the most likely location of a downstream cyclogenesis.

## 2.3 Tracking the influence of observations

The concept of downstream development has been used routinely at ECMWF to track the origin of serious medium-range forecast errors due to analysis errors (Persson 2000). The algorithm is based on the realization that the time evolution of a signal initially confined to the region of an atmospheric wave packet must be qualitatively similar to that of the wave packet. Hence, the propagation of the leading edge of the signal can be deduced from the predicted or observed propagation of the wave packet. This technique has been used successfully for years at ECMWF.

The original motivation to collect targeted observations was the notion that strongly localized (in physical space) analysis error patterns can cause potentially serious forecast errors. These important initial error patterns were identified by adjoint sensitivity gradients (e.g. Rabier et al. 1992,1996, Errico et al. 1993, Langland et al. 1996), singular vectors (e.g. Palmer et al. 1998, Buizza and Montani 1999), or Lyapunov/bred vectors (Toth and Kalnay, 1993,1997). It has been well known that the evolution of the dominant singular vectors (Hartmann et al., 1995, Hoskins et al. 2000) and Lyapunov/bred vectors (Szunyogh et al. 1997) is strongly related to baroclinic wave development. Toth et al. (1997) also showed that the difference between two perturbed ensemble forecasts traveled, from the East Pacific to the region of The Blizzard of '93 over the Eastern United States, at a speed much faster than the phase velocity of the individual waves. The experience that the dynamical influence could successfully be traced by the difference between two bred ensemble perturbations suggested that an ensemble-based technique could potentially be used in the sensitivity analysis step of targeting. This observation eventually led to the development of the ET and the ETKF techniques by collaborating researchers at Penn State University and NCEP.

# 3 The WSR00 data set

## 3.1 The WSR00 field program

The ETKF attempts to predict the reduction in forecast error variance within a verification region due to a specific deployment of the targeted observations, such as a flight track. 23 (19) flight tracks were designed out of Anchorage (Honolulu) prior to the beginning of WSR00 and the one that maximized the predicted error reduction on a given day for the selected weather events was deemed optimal. The weather events were selected by the operational forecasters at the Hydrometeorological Prediction Center (HPC) of NCEP and the ETKF calculations were made based on operational ensemble forecast products from NCEP (Toth and Kalnay, 1997) and ECMWF (Buizza et al., 1998).

The observational time ($t_o$), the verification time ($t_v$) and the center of the 1000 km radius verification region for the individual targeting events in WSR00 are given in Table 1. Altogether, nearly 300 dropsondes were released (about 200 fewer than during WSR99) from 15 flights on 12 separate days. The missions involved flights with two planes: a United States Air Force Reserve C-130 plane flying out of Honolulu, Hawaii and a Gulf-stream G-IV jet, operated by the National Oceanic and Atmospheric Administration (NOAA), and stationed in Anchorage, Alaska. The latter aircraft was available only until 9 February.

One flight (C-130, 23 January) could not be completed as planned due to problems with the airplane. Observations were also taken on three ferry flights (25 January, 1 and 16 February). The tracks for these flights were designed with the aim of providing acceptable data coverage of the most sensitive regions without increasing the cost of the flights. The dropsonde locations, combined for the 12 flight days, are shown in Figure 1.

## 3.2 The analysis-forecast cycles

All dropsonde data were assimilated in real time by the Spectral Statistical-Interpolation (Parrish and Derber, 1992 and Parrish et al., 1997), a three-dimensional variational assimilation scheme, into the operational NCEP global model products. In this study, only forecasts from the low horizontal resolution (T62) global analysis/forecast cycle are considered. In order to evaluate the effect of the dropsonde data, an additional analysis-forecast cycle was run in parallel to the operational cycle. This parallel *control cycle* was identical to the operational cycle, except no dropsonde data were assimilated. Based on earlier experience (SEA), it was expected that targeted observations would have the largest influence on forecasts initiated at the actual observational time, but forecasts issued later were also expected to show a lesser impact as a results of the cycling of the analysis.

It is important to note that there were no major changes in the NCEP global analysis-forecast system between January-February 1999 (WSR99) and January-February 2000 (WSR00). Neither were there major changes in the targeting technique. Therefore, any qualitative difference between results from

| flight date | region | latitude | longitude | max $p_s$ [hPa] | max $\mid \mathbf{v} \mid$ [m/s] |
|---|---|---|---|---|---|
| 2301G+C | A24 | 60.0 | 150.0 | 2 | 15 |
| | E72 | 30.0 | 90.0 | | |
| 2501C | E48 | 37.5 | 75.0 | 1 | 10 |
| 2601G | A24 | 60.0 | 150.0 | 2 | 30 |
| | A48 | 60.0 | 150.0 | | |
| 2801G+C | W48 | 50.0 | 125.0 | 2 | 25 |
| | E84 | 37.5 | 75.0 | | |
| 3001G+C | W48 | 45.0 | 125.0 | 3 | 15 |
| 0102C | W24 | 45.0 | 125.0 | 4 | 25 |
| | E72 | 32.5 | 87.5 | | |
| 0202C | E60 | 27.5 | 80.0 | 3 | 30 |
| 0902G | E60a | 40.0 | 95.0 | 2 | 25 |
| | E60b | 45.0 | 75.0 | | |
| | E84 | 45.0 | 75.0 | | |
| 1102C | W24 | 37.5 | 122.5 | 2 | 10 |
| | E48 | 40.0 | 80.0 | | |
| 1302C | W36 | 37.5 | 122.5 | 1 | 10 |
| | E48 | 40.0 | 75.0 | | |
| 1402C | W24 | 40.0 | 122.5 | 1 | 10 |
| | E48 | 45.0 | 87.5 | | |
| | E72 | 42.5 | 75.0 | | |
| 1602C | W24 | 37.5 | 120.0 | 1 | 10 |
| | E48 | 37.5 | 95.0 | | |

Table 1: List of the 12 targeted observational days (first column). The first two digits define the day, while the second two digits the month. G, C, and G+C, respectively, denote flights with the Gulf-stream G-IV jet, with the C-130 aircraft, and with both planes at the same time. Each of the 23 WSR00 targeted forecast cases are marked by a one letter identifier of the region and the forecast lead time (column 2). The letters A, E, and W stand for Alaskan, west coast, and east coast verification regions, respectively. The coordinates of the center of these regions are listed in columns 3 and 4. The largest change in the analysis of the surface pressure (300-hPa height) is shown in column 5 (6). Values in the last two columns are rounded to the closest integer.

the WSR99 and the WSR00 programs, apart from sampling fluctuations due to the limited number of cases, can be attributed to the differences between the flow regimes of the different years.

# 4 The atmospheric flow during WSR00

## 4.1 The large scale flow

Diagnostics shown for the Northern Hemisphere flow regimes are based on the the 0000 and 1200 UTC T62 horizontal resolution operational global NCEP analyses. The 30-day mean of the 300-hPa geopotential height is shown for both WSR99 and WSR00 (Figure 1) to highlight differences in the large scale flow of the two field programs. During WSR00, the well pronounced trough of WSR99 was replaced by a ridge over the Bay of Alaska and the Icelandic trough extended much deeper into eastern Canada and the north-eastern United States. Regarding the three main areas in which the forecasts were to be improved, the flow was southwesterly over Alaska and the west coast and northwesterly over the eastern United States. During WSR00 all flights leaving from or returning to Honolulu, and all but two flights out of Anchorage targeted the region between the Aleutian low and the weak stationary ridge over the west coast.

## 4.2 Wave packets

To diagnose transient features of the atmospheric flow, techniques developed by Orlanski and Katzfey (1991); Chang and Yu (1999); and Chang (1999) are applied. These diagnostics are based on eddy quantities defined by the deviation from the 30-day time mean and include the method of *complex demodulation* and the computation of the dominant terms in the *eddy kinetic energy budget equation*. Maps were plotted based on each 0000 and 1200 UTC analysis with the aim of exploring the relationship between eddies and the propagation of the dropsonde impact in each individual case. This is in contrast to the approach of SEA that investigated the relationship mainly based on time and composite means.

The method of complex demodulation (Bloomfield, 1976), first suggested by Chang and Yu (1999) for tracking upper tropospheric wave packets, locates wave packets by extracting the packet envelope function. In this study we use a variant of the technique, explained in detail by A. Zimin et al. (manuscript is submitted to J. Atmos. Sci. and available from the corresponding author), which assumes that the eddy component of the meridional wind, $v'(x)$, along a given latitude can be expressed in the form

$$v'(x,t) = \sum_k A_k(x,t) cos(kx + \phi_k). \tag{6}$$

Here the sum is taken over those wavenumbers, $k$, in the range from 5 to 10, for which the maximum of the packet envelope, $A_k(x,t)$, exceeds a given threshold.

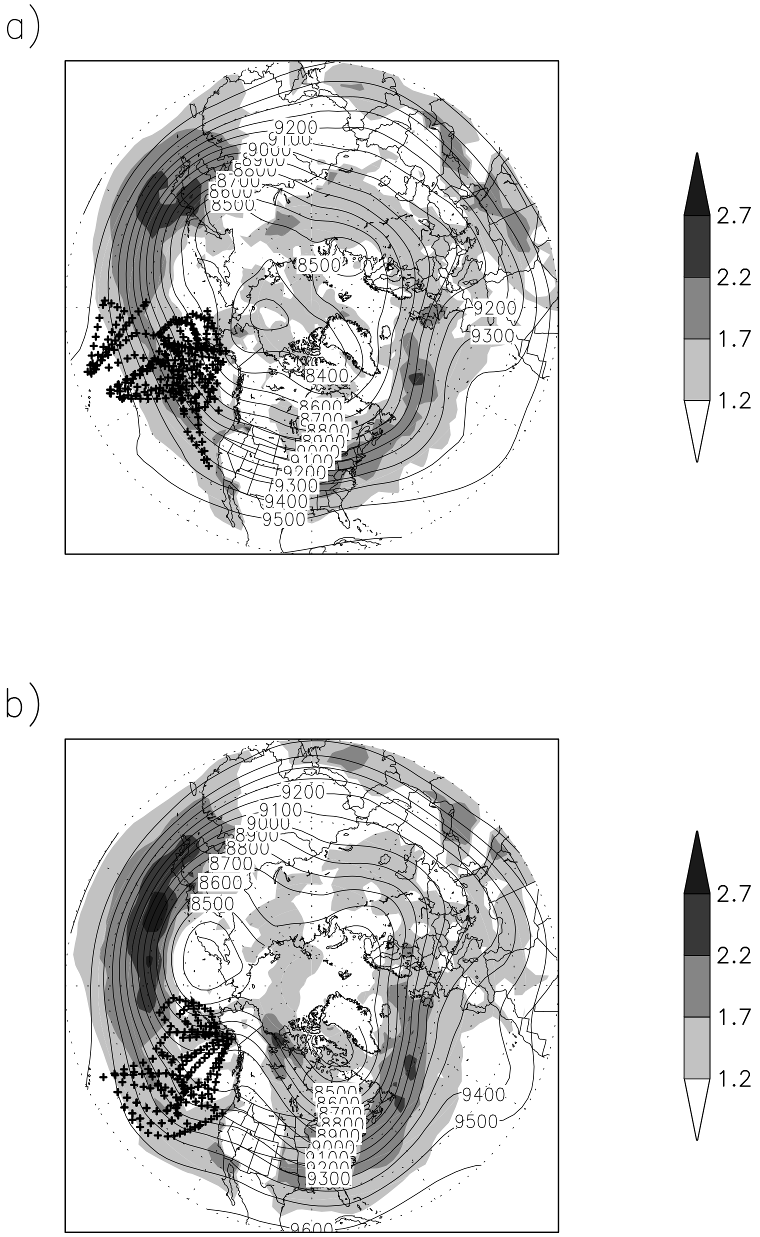

Figure 1: The time-mean geopotential height of the 300-hPa surface for WSR99 (a) and for WSR00 (b). The sample period starts at 13 January 1999 0000 UTC for WSR99 and at 23 January 2000 0000 UTC for WSR00. Shown by shades is the daily amplification of the most unstable baroclinic mode (Eady index) for the time-mean flow in the 850-925 hPa layer. Dropsonde locations are shown by crosses.

The packet envelope is then visualized by taking the root-mean-square of the amplitudes $A_k(x,t)$ over the different wave numbers.

An example for the wave packet analysis is shown in Figure 2. This figure shows the time evolution of the wave packet for the 84-hour period started at 25 January 2000 0000 UTC. At the beginning, the packet envelope extended from the region of a trough located over the eastern Pacific to the southeastern states of the United States. Then the wave packet moved first toward the east and then to the north mainly following the direction of the geostrophic wind.

The packet envelope amplified explosively over the east-coast during the first 24 hours. This cannot be explained without investigating the dominant terms in the equation that governs the time evolution of the vertically averaged eddy kinetic energy (Orlanski and Katzfey 1991)

$$K = \frac{1}{(p_s - p_t)} \int_{p_t}^{p_s} \frac{1}{2}(u'^2 + v'^2), \tag{7}$$

where $u'$ is the eddy component of the zonal wind, $p_s$ is the surface pressure, and $p_t$ is 100 hPa. The three terms we are most interested in are the vertical average of the *baroclinic energy conversion*, $(\omega'\alpha')$; the *convergence of ageostrophic geopotential fluxes*, $(\mathbf{v}_a{}'\phi')$; and the *barotropic energy conversion* associated with the horizontal deformation in the large scale flow, $(\mathbf{v}'\cdot\overline{(\mathbf{v}'\cdot\nabla)\mathbf{v}'}) - (\mathbf{v}'\cdot(\mathbf{v}'\cdot\nabla)\bar{\mathbf{v}})$. Here, $\omega'$, $\alpha'$, $\mathbf{v}_a{}'$, and $\phi'$ are, respectively, the eddy components of the vertical velocity in pressure coordinate system, the specific volume, the ageostrophic wind component, and the geopotential height. The overbar denotes the time mean.

The importance of the baroclinic energy conversion term is obvious and its use in our analysis requires no further justification. The second term, the convergence of the ageostrophic geopotential fluxes, is thought to explain the mechanism through which upper tropospheric wave packets can trigger downstream baroclinic development (Orlanski and Sheldon, 1993 and 1995). This means that targeting a far upstream region can be expected to have significant influence on the weather downstream only at times and locations where this term plays an important role. Finally, investigating the third term will enable us to verify that the energy of the propagating waves is not lost to negative barotropic energy conversion. The eddy kinetic energy and the energy flux $(-\nabla(\mathbf{v}K))$ were also plotted to verify the results obtained by complex demodulation. These figures are not shown due to the good agreement with Figure 2.

Figure 3 shows that the amplification of the packet envelope is the result of strong baroclinic energy conversion. This strong energy conversion started after the leading edge of the wave packet reached the baroclinically unstable region and the convergence of ageostrophic fluxes started generating eddy kinetic energy off-shore of the southeastern states(Figure 4). While this term continued to play an important role in the local energetics at the leading edge of the wave packet, it also continued to transport energy to the east-coast region for two more days. Brief descriptions of the targeted synoptic/dynamic features for the twelve WSR00 cases are presented in the Appendix, based on figures similar to Figure 2-4.

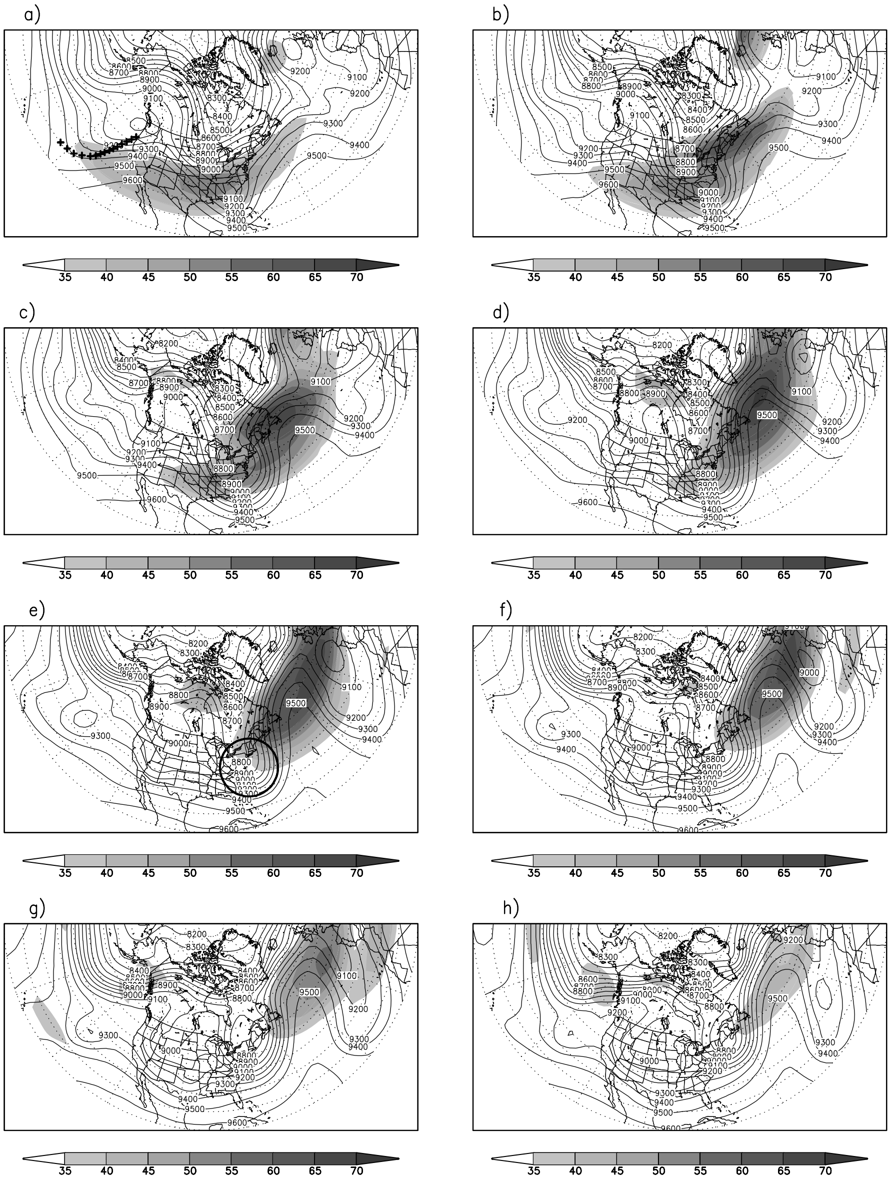

Figure 2: Shown by shades is the wave packet envelope function at 25 January 0000 UTC (a), at 25 January 1200 UTC (b), at 26 January 0000 UTC (c), at 26 January 1200 UTC (d), at 27 January 0000 UTC (e), at 27 January 1200 UTC (f), at 28 January 0000 UTC (g), and at 28 January 1200 UTC (h). Contour lines show the proper lead time analysis of the 300-hPa geopotential height. Crosses show the dropsonde locations and the ellipse in panel (e) shows the verification region for the targeting mission on 25 January 0000 UTC.

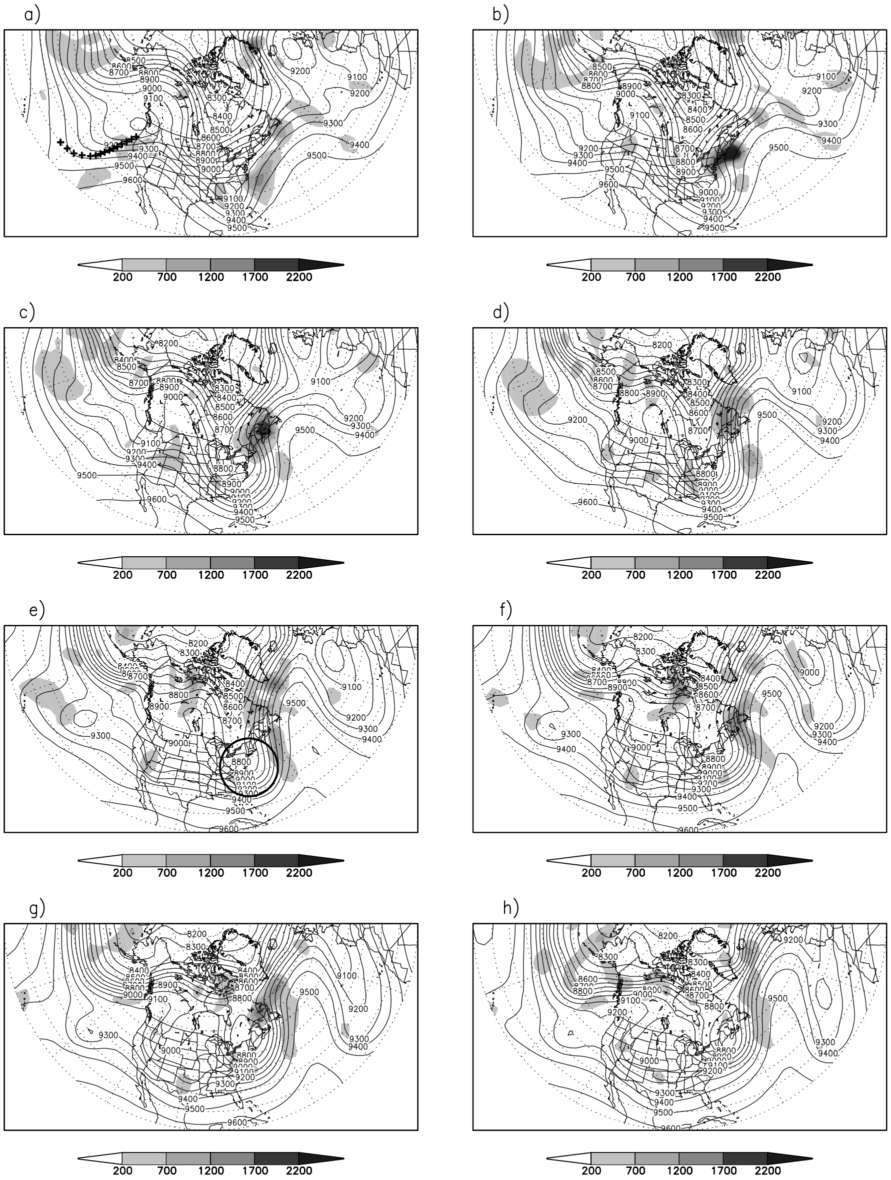

Figure 3: Same as figure 2, except shown by shades is the baroclinic energy conversion.

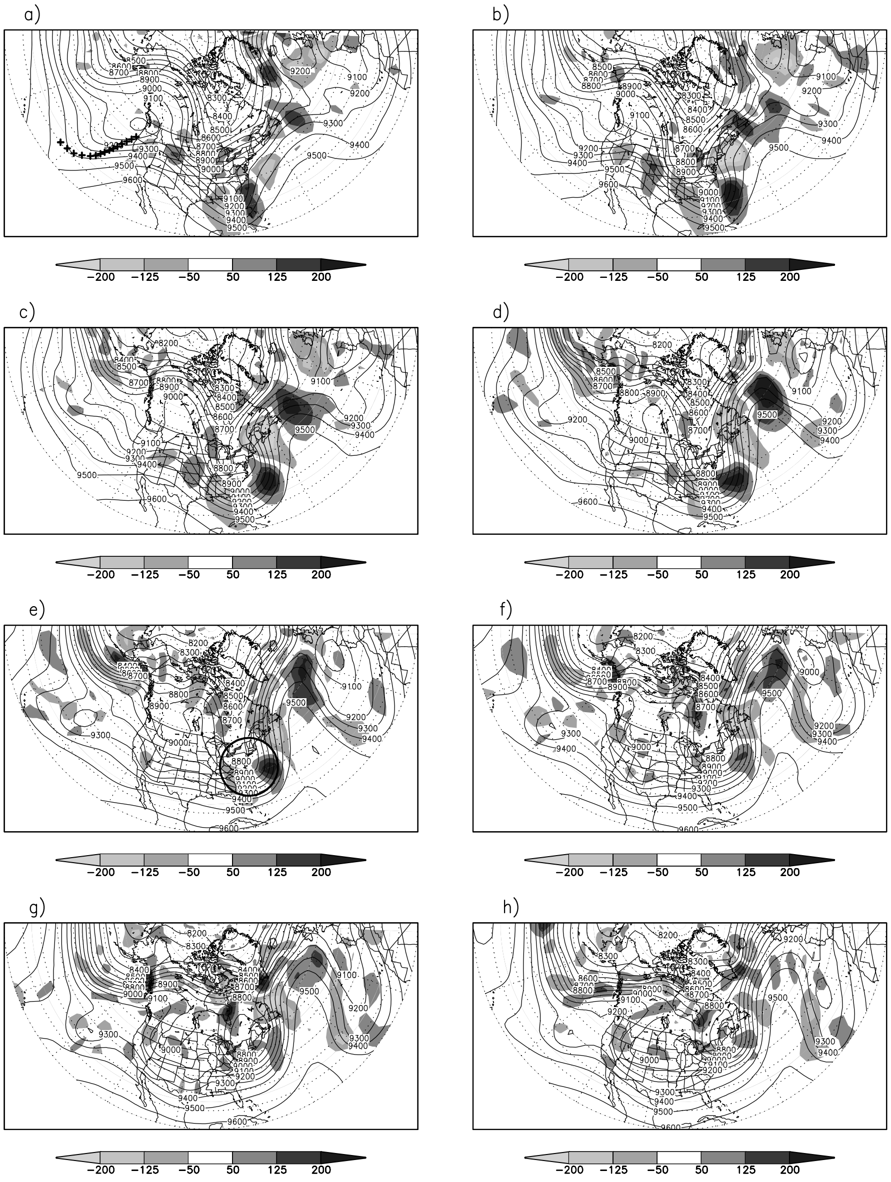

Figure 4: Same as figure 2, except shown by shades is the convergence of the ageostrophic geopotential fluxes.

# 5 Propagation of the influence of targeted observations

## 5.1 Indivdual targeting cases

To explore the relationship between the atmospheric flow and the propagation of the dropsonde impact, an additional pair of figures was also drawn for each case. These figures show the 300-hPa geopotential height and the surface pressure differences between the operational and the control forecasts started at $t_o$. An example is presented in Figures 5 and 6 for the flight mission that was flown centered around January 25 0000 UTC. The aircraft flew from the warm advection side to the center of the upper level wave and the dropsondes sampled the trailing edge of the wave packet. This led to a 12 meter increase in the geopotential height at the location of the maximum impact. The negative barotropic energy conversion (not shown) was strong in the targeted region, but it played no role in the area along which the signal propagated to the east. The leading edge of the difference between the two forecasts in the upper troposphere traveled with the trailing edge of the wave packet at a speed of nearly $30^o/day$; the leading edge of the data impact reached the first crest after 12 hours and the next downstream trough after 24 hours.

At the surface, the influence of the added data followed the regions of maximum changes in the upper troposphere with a 12-24 hours delay. Within the verification region, there is a clear relationship between the impact of the data and the local energetics; the largest change in the surface pressure forecast, as well as a strong local maximum at the 300-hPa pressure level, is at the location of a strong local maximum in the convergence of the ageostrophic geopotential fluxes. It can be concluded that the ETKF identified a causal relationship between an upper tropospheric wave packet over the northeast Pacific at 25 January 0000 UTC and a downstream energy conversion process over the east-coast of the United States at 27 January 0000 UTC.

The results of the case studies, based on figures similar to those shown in the above example, are summarized in Tables 2 and 3, and Figure 7. Figure 7 is a Hovmöller diagram (Hovmöller, 1949) plotted for the eddy component of the meridional wind at the 300-hPa pressure level in the the 30N-60N latitude band. The meridional integral of the packet envelope function for the same channel is also shown. A downstream propagating wave packet in this diagram can be recognized either by a series of alternating positive and negative contours for the eddy component of the wind or by large values of the packet envelope function. Both run along diagonal lines from the top left to the bottom right direction. The dropsonde locations are marked by crosses, while the center of the verification regions are marked by circles and squares. Thin lines connect the centers of the observational and verification regions and their slope is proportional to the signal velocity as predicted by the ETKF technique for the flight days.

The targeting cases form two groups distinguished by the targeted synoptic features. Ten cases belong to the first group, for which storms that later reached

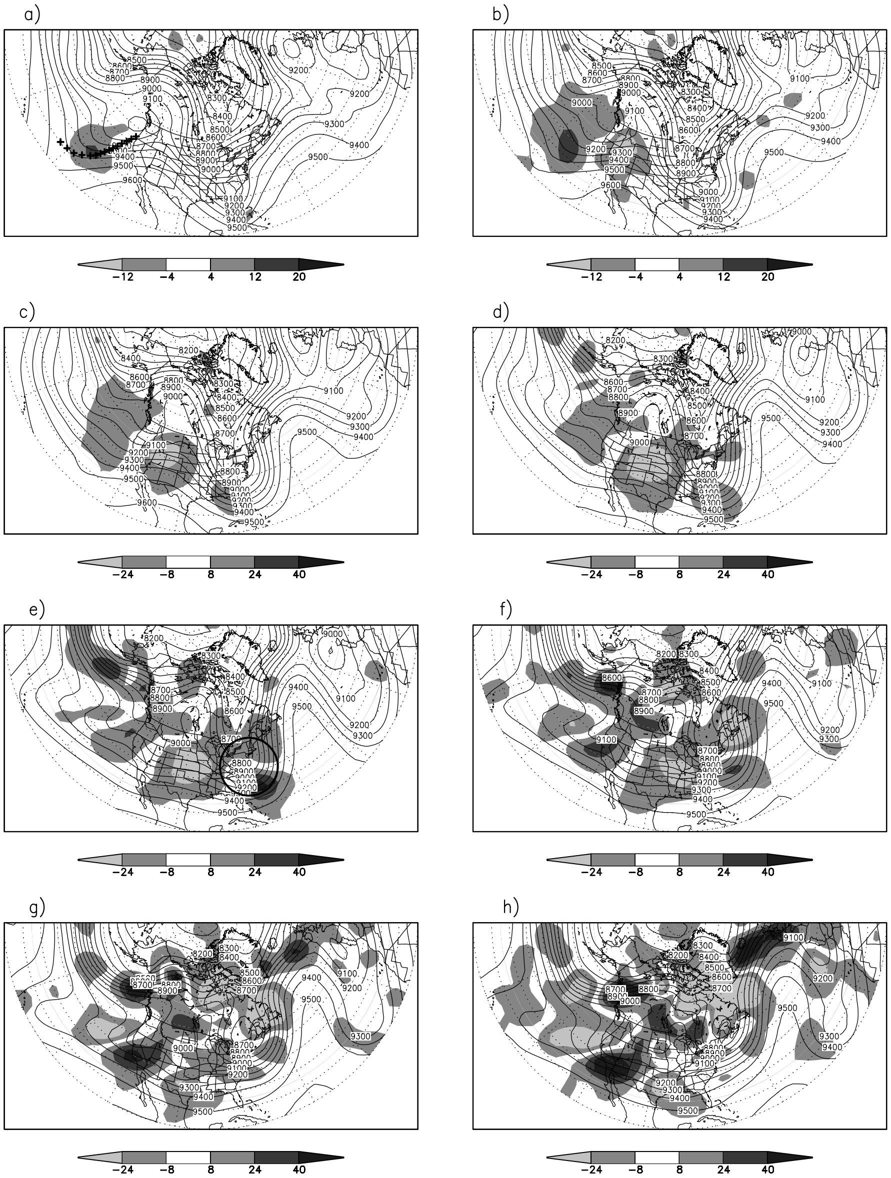

Figure 5: The difference between the operational and the control forecasts initiated at 25 January 0000 UTC at analysis time (a), at 12 h (b), at 24 h (c), at 36 h (d), at 48 h (e), at 60 h (f), at 72 h (g), and at 84 h (h) (shades). Contour lines show the proper lead time forecasts of the 300-hPa geopotential height. Crosses show the dropsonde locations and the ellipse in panel (e) shows the verification region.

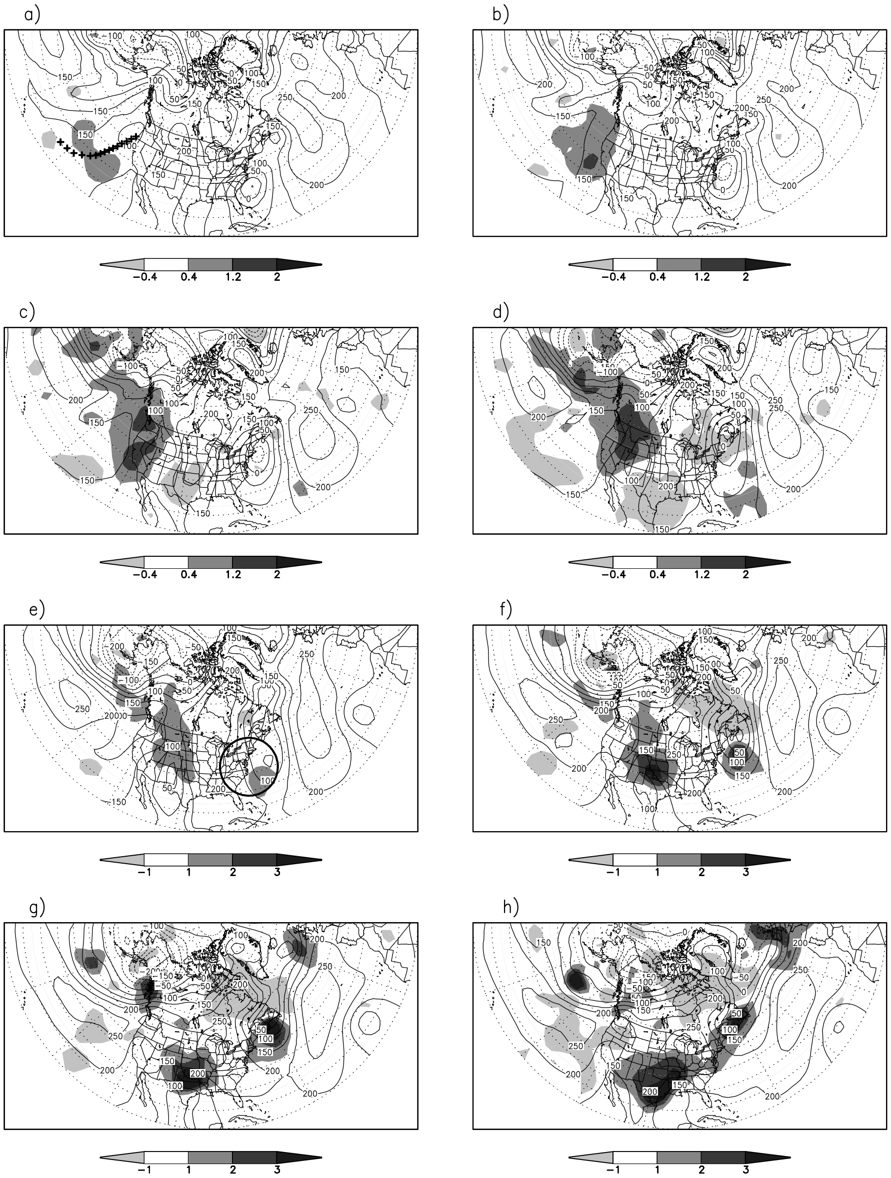

Figure 6: Same as Figure 5 except for the surface pressure difference (shades) and the 1000-hPa geopotential height forecasts (contour).

| flight date | region | K $[m^2/s^2]$ | $-\nabla(\mathbf{v}_a{}'\phi')$ $[m^2/s^3]$ | $\omega'\alpha'$ $[m^2/s^3]$ | max $p_s$ [hPa] | max $z_{300}$ [gpm] |
|---|---|---|---|---|---|---|
| 2301G+C | A24 | weak | no | modest | 3 | 15 |
| 2601G | A24 | modest | strong | no | 5 | 50 |
|  | A48 | strong | strong | modest | 4 | 30 |
| 2801G+C | W48 | modest | strong | strong | 5 | 30 |
| 3001G+C | W48 | modest | strong | strong | 2 | 10 |
| 0102C | W24 | modest | strong | weak | 2 | 35 |
| 1102C | W24 | modest | weak | no | 3 | 30 |
| 1302C | W36 | modest | no | modest | 2 | 20 |
| 1402C | W24 | weak | no | no | 1 | 20 |
| 1602C | W24 | modest | strong | weak | 0 | 20 |

Table 2: The forecast effect of the targeted data in the west-coast and Alaskan verification regions. The first two columns are the same as in Figure 1. The eddy kinetic energy (column 3) is said to be strong (modest, weak) if it is larger than 1600 (800, 400) $m^2/s^2$. The same categories for the convergence of the ageostrophic geopotential fluxes (column 4) are defined by the thresholds 200, 125 and 50 $m^2/s^3$, while for the baroclinic energy conversion (column 5) by the thresholds 800, 400, and 100 $m^2/s^3$. The maximum local change in the surface pressure (300-hPa geopotential height) forecast within the verification region is shown in column 6 (7). Values in the last two columns are rounded to the closest integer.

| flight date | region | K $[m^2/s^2]$ | $-\nabla(\mathbf{v}_a{}'\phi')$ $[m^2/s^3]$ | $\omega'\alpha'$ $[m^2/s^3]$ | max $p_s$ [hPa] | max $z_{300}$ [gpm] |
|---|---|---|---|---|---|---|
| 2301G+C | E72 | modest | strong | weak | 1 | 30 |
| 2501C | E48 | strong | strong | modest | 2 | 40 |
| 2801G+C | E84 | modest | weak | modest | 1 | 0 |
| 0102C | E72 | no | no | no | 0 | 60 |
| 0202C | E60 | no | no | no | 0 | 20 |
| 0902G | E60a | no | no | weak | 2 | 25 |
|  | E60b | modest | no | modest | 1 | 5 |
|  | E84 | no | no | modest | 4 | 40 |
| 1102C | E48 | no | no | weak | 0 | 10 |
| 1302C | E48 | modest | weak | strong | 2 | 30 |
| 1402C | E48 | modest | weak | modest | 1 | 20 |
|  | E72 | modest | weak | modest | 2 | 60 |
| 1602C | E48 | no | weak | modest | 0 | 10 |

Table 3: Same as table 2 but for the east-coast verification regions.

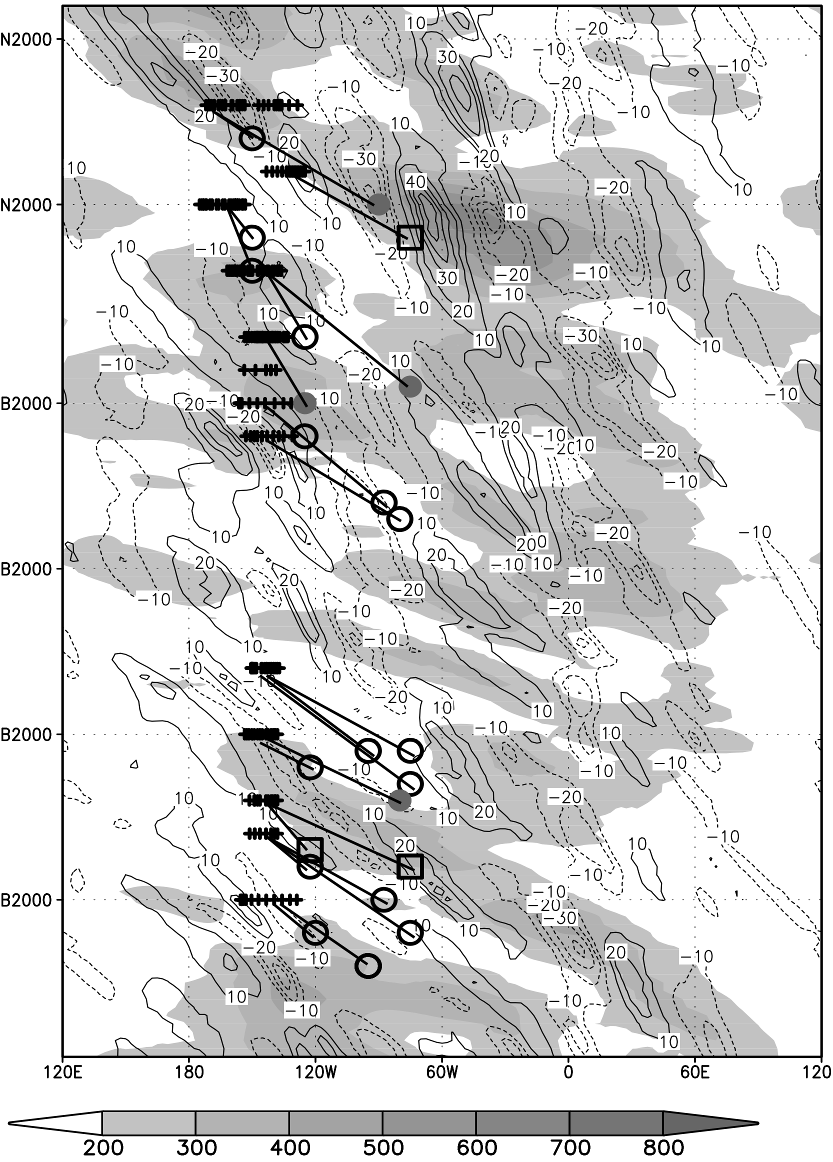

Figure 7: Hovmöller diagram (time-longitude cross section) for the meridional mean of the meridional wind component between 30N and 50N at the 300-hPa pressure level. Contour interval is 10 m/s. Shaded areas show the regions where the meridional sum of the packet envelope function has maxima. The dropsonde locations are shown by crosses. Open circles, closed circles, and open squares identify, respectively, the center of the verification regions for cases where the quality of the forecast within the verification region was improved, was not changed, and was degraded.

the west-coast were observed over the northeast Pacific. The lines that mark the expected signal propagation for these cases in the Hovmöller diagram do not cross through regions of both negative and positive meridional wind anomalies. This group consists of very different targeting cases, despite the fact that at targeting time barotropic energy conversion played an important role at targeting time in each of them. In four cases strong baroclinic energy conversion was observed (see 2301 A24; 2601 A24 and A48; 0102 W24 in Table 1 and Appendix); in one case data were collected in the region of a shallow wave that later deepened through the convergence of ageostrophic geopotential fluxes and baroclinic energy conversion (2801 W48); an other case sampled a mature cyclone that rapidly weakened through negative barotropic energy conversion(3001 W48); and four others took observations of different amplitude waves associated with modest or weak baroclinic energy conversion (1102 W24; 1302 W36; 1402 W24; 1602 W24). Based on the results, summarized in the Appendix and Table 2, the data tended to have the largest impact in those cases when baroclinic energy conversion was strong at some stage of the signal propagation and the convergence of the ageostrophic geopotential fluxes was strong at verification time.

The second group consists of targeting cases with east-coast verification regions. Barotropic energy conversion played an important role at the targeting time for these cases, too, but it had no impact during the propagation of the signals over the United States. Figure 7 demonstrates that downstream propagating wave packets helped the ETKF technique in finding the observational locations, although there are obvious mismatches between the propagation of the wave packets and the expected tracks of the signal. Notably, (1) observations were taken in the region of a wave with no associated wave packet on 9 February; and (2) the missions 2801 E84 and 1102 E48, for which the verification regions were too far to the south and east of the wave packet. This shows that selecting east-coast verification regions, based on forecasts that are sometimes as long as 132 hours, can be difficult when nonzonal large scale flow prevails over the north-east Pacific.

Nevertheless, the prediction of the ETKF proved to be correct on most occasions in that the influence of the dropsondes reached the verification region at the expected time in the upper troposphere. The only exceptions are the aforementioned 2801 E84 and 1102 E48 cases. For the flight on 9 February, however, the dropsonde signal reached two of the three verification regions as predicted. This indicates that the upper tropospheric propagation of the dropsonde impact is governed by the basic flow and the influence of the added data shows wave type propagation even if atmospheric waves are not present. This is in agreement with the theoretical considerations of section 2.

There were three other cases (0102 E72; 0202 E60; 1102 E48) when reasonable upper tropospheric impact was observed, but the forecast effect at the surface was negligible. The common feature of these cases is the insignificant divergence of ageostrophic fluxes in the verification region, which is a clear indication that downstream baroclinic energy conversion did not take place. There was only one case (1602 E48) when the divergence of ageostrophic geopotential fluxes was weak, but not negligible, and forecast changes at the surface still could not be detected. In this case, however, the coverage of the targeted wave at observational time was far from optimal (see Appendix).

### 5.2 Evolution of the composite mean signal

In this section, the propagation of the dropsonde impact is further investigated by exploring the spatio-temporal evolution of the composite mean signal. The advantage of this approach is that the composite mean filters out a large part of the dynamical noise inherently present in the individual cases and it also helps the detection of changes in the time mean flow. The time evolution of the composite mean of the 300-hPa geopotential height and surface pressure signal is shown in Figure 8. The most striking feature is the large local surface pressure impact in the region of the stationary surface low.

During the first 48 hours, the leading edge of the signal at 300 hPa height traveled about $60^o$ along the southern branch of the jet. This indicates a $30^o$/day average propagation speed, which is similar to the average group velocity of the upper tropospheric wave packets. In the same region, the surface pressure impact propagates with distinct 'jumps' to the east: local maxima in the surface pressure signal are separated by areas of no-significant impact. A comparison of Figure 8.h and the energy conversion terms revealed that, as expected, the local maxima of the surface pressure composite mean signal built up in regions where the wave packets went through strong energy conversions.

The causal relationship between changes in the analyses and the forecasts was further investigated by plotting correlation maps (not shown), prepared for two base points, one along the southern branch of the flow at 40N, 140W and another along the northern branch of the flow at 45N, 175W. The correlation between the surface pressure change at the selected base points at analysis time and the surface pressure change at each point in the Northern Hemisphere extra-tropics was computed at different forecast lead times over all 12 cases. The regions occupied by points characterized by high correlations were found to be strongly localized. For the base point at 40N, 140W the large correlation areas (defined by larger than 0.8 absolute value) are over the northeast Pacific for the first two days and then a large positive correlation area develops with a sudden jump over the eastern states of the United States and the west Atlantic. For the base point at 45N, 175W the large (positive) correlation area is over the Aleutian Islands at 24 h and over Alaska at 48 h forecast times.

## 6 The analysis-forecast effects of targeted data

### 6.1 Effects on the analyses

The goal of targeting weather observations is to improve forecasts through making better initial weather analyses. In principle, all dropsonde data collected at and before an actual flight day can contribute to the difference between the qual-

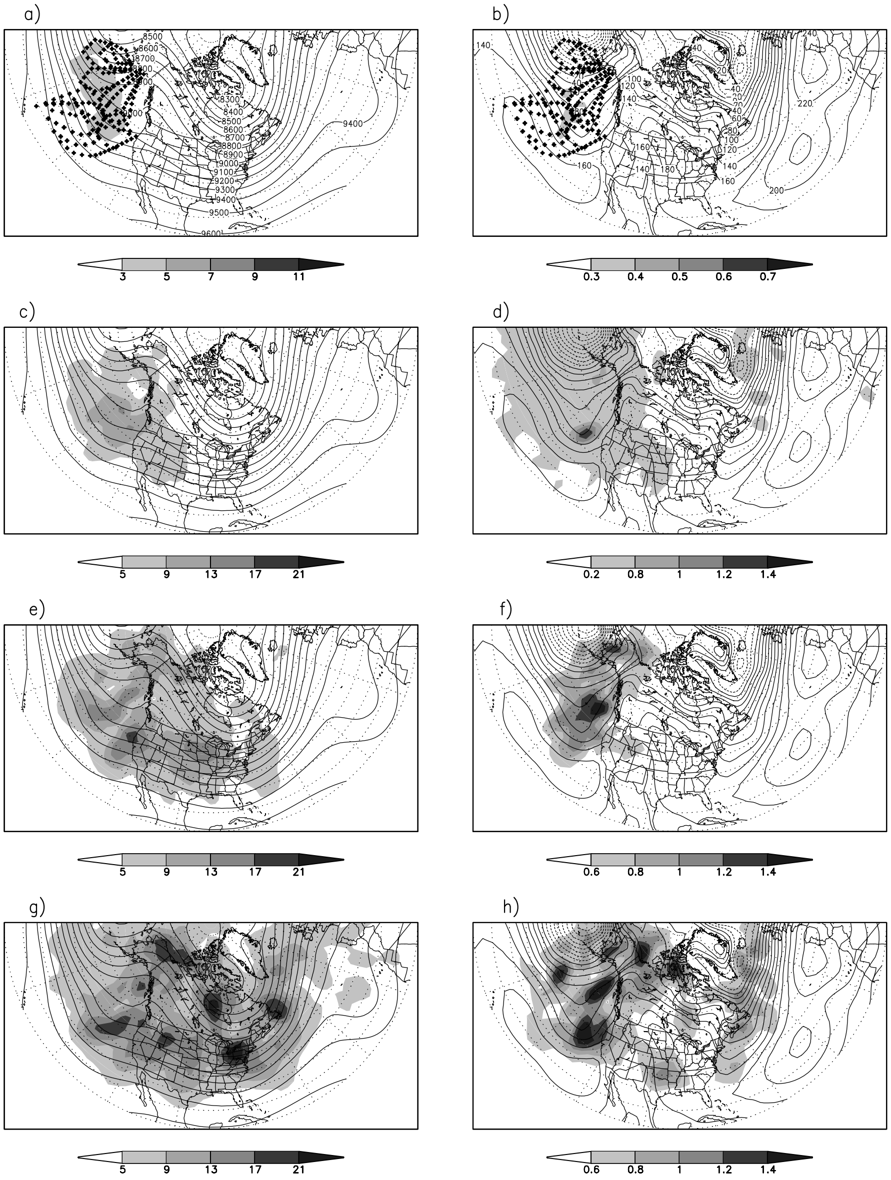

Figure 8: Composite mean of the geopotential height [*gpm*] signal (shades) at the 300-hPa pressure level (a, c, e, g) and for the surface pressure (b, d, f, h) at analysis time, 24-, 48-, and 72-h lead times, respectively. Contours show the time-mean of the geopotential height analyses in WSR00 at the 300-hPa (a, c, e, g) and the 1000-hPa (b, d, f, h) pressure levels.

ity of the operational and the control analyses due to the cycling of the data assimilation. Figure 8 shows, however, that the major analysis impact was typically concentrated around the region targeted by the dropsonde observations. We also note that the rms fit of the background forecasts to the statistically independent dropsonde data was usually not better in the operational than in the control cycle. Changes in the quality of the analyses, therefore, can be attributed to data collected at the latest analysis time. This is in contrast to the results reported for WSR99 (SEA), where it was shown that the background forecasts better fitted the data in the operational than in the control cycle on all but two occasions, with an average of 6 % improvement in the fit to the data.

## 6.2 Verification of forecasts against data

In this section, verification statistics are compared for forecasts from the operational and the control cycles. Each forecast is verified against all available traditional (not remote sensed) observed data within the verification regions. Since both sets of forecasts are verified against the same large set of observed data, changes in the forecast quality that are much smaller than the errors in the individual observations can be detected (see Appendix in SEA for more details). The verification results are presented in Table 4 and by Figure 9. Symbols over the $45^o$ line in the scatter plots of Figure. 9 indicate forecast improvement, while symbols under the same line show forecast degradation.

The overall quality of the forecasts with the targeted data improved (remained neutral) in 62.5% (24.5%) of the cases, while degradations were observed only in 13% of all cases. Targeted data had the highest positive impact on the quality of surface pressure forecasts (70% improvement, 21% neutral, 9% degradation) reducing the average error in the verification regions by 19% (from 3.635 hPa to 2.948 hPa). Importantly, whenever there was a reasonable change in the surface pressure forecast, the change in its quality was always positive and the larger than 4 hPa control forecast errors were always reduced. Concerning the wind forecasts, the largest improvements also occurred in the large error cases (larger than 10 m/s), but in three large error cases the forecast error was not reduced. Overall, 65% (35%) of the wind forecasts showed an error reduction (increase).

There was also a close relationship between the change in the quality of the forecast and the type of meteorological feature that the added data targeted. When the reduction in the surface pressure error is measured by the ratio of the error reduction and the error in the control forecast, the three largest improvement cases are those associated with land-falling systems characterized by strong baroclinic energy conversion at the targeting times, and by strong convergence of ageostrophic fluxes at verification times (0102 W24: 58%; 2601 W24: 48%; 2601 W48: 29%).

| flight dates | $t_v$-$t_o$ [h] | $p_s$ error [hPa] op./cont. | $\mid \mathbf{v} \mid$ error [m/s] op./cont. | overall effect |
|---|---|---|---|---|
| 2301G+C | A24 | 2.6/2.6 | 9.3/9.4 | + |
| | E72 | 2.0/2.1 | 9.6/9.4 | 0 |
| 2501C | E48 | 3.0/3.0 | 7.5/6.7 | - |
| 2601C | A24 | 2.2/4.2 | 9.1/12.7 | + |
| | A48 | 5.3/7.5 | 8.3/8.4 | + |
| 2801G+C | W48 | 2.0/2.7 | 9.5/9.8 | + |
| | E84 | 6.9/7.8 | 13.0/12.3 | 0 |
| 3001G+C | W48 | 1.9/2.4 | 12.6/11.9 | 0 |
| 0102C | W24 | 1.0/2.4 | 11.3/12.9 | + |
| | E72 | 7.8/8.4 | 11.4/13.9 | 0 |
| 0202C | E60 | 2.9/3.3 | 9.1/9.6 | + |
| 0902G | E60a | 5.0/5.5 | 7.9/8.9 | + |
| | E60b | 3.2/3.3 | 2.3/2.4 | 0 |
| | E84 | 2.6/2.8 | 8.0/8.7 | + |
| 1102C | W24 | 3.2/3.2 | 7.5/8.1 | + |
| | E48 | 2.6/2.7 | 8.2/7.6 | 0 |
| 1302C | W36 | 3.6/3.4 | 12.1/11.8 | - |
| | E48 | 2.2/1.8 | 11.7/9.1 | - |
| 1402C | W24 | 0.9/1.2 | 8.0/9.4 | + |
| | E48 | 2.3/2.5 | 9.5/10.5 | + |
| | E72 | 4.2/4.6 | 11.3/13.1 | + |
| 1602C | W24 | 3.2/3.2 | 7.6/7.7 | + |
| | E48 | 3.0/3.0 | 7.1/7.3 | + |
| wins/losses | | 16/2 | 15/8 | 15/3 |

Table 4: The effect of the targeted data on forecast quality. The first two columns identify the cases as in earlier figures. The rms surface pressure and 300-hPa geopotential height forecast error within the verification region for the operational/control forecasts is shown in columns 3 and 4. The overall forecast improvement (degradation, neutral impact) is shown by a + (-,0) sign depending on whether both individual measures in columns 3 and 4 are positive (negative, mixed).

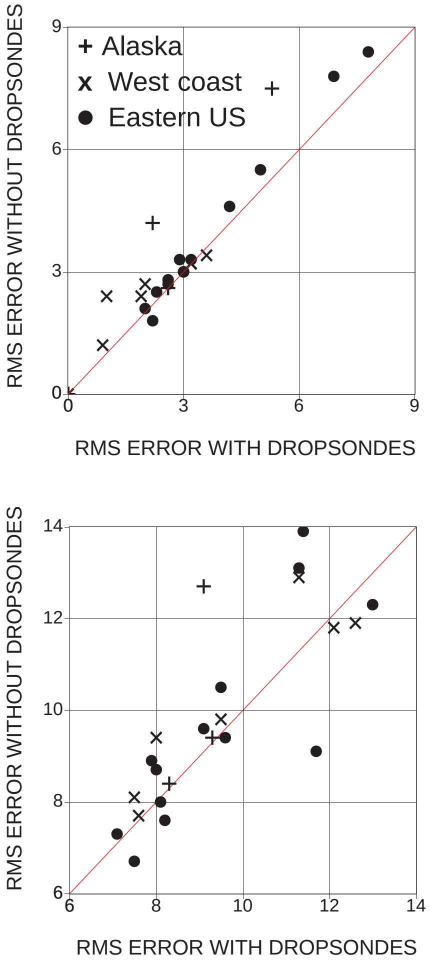

Figure 9: RMS error (measured against observations) in the surface pressure (a) and winds forecasts (b) for the operational (horizontal axis) and the control (vertical axis) forecasts in the defined west coast (dots), east coast (crosses) and Alaskan (plus signs) verification regions.

## 6.3 Propagation of the forecast error

The spatio-temporal evolution of the forecast improvement cannot be evaluated without exploring the spatio-temporal evolution of the forecast error in the control cycles. The composite mean of the analysis based estimate of the local forecast error is defined by

$$\frac{1}{12}\sum_{i=1}^{12} \mid {f_i}^c - {a_i}^c \mid, \tag{8}$$

where ${f_i}^c$ is the control forecast initiated on the *ith* flight day and ${a_i}^c$ is the verifying analysis from the same cycle. The geographical distribution of the quantity defined by Eq. 8 is shown for the 300-hPa geopotential height and surface pressure at forecast lead-times 24- 48- and 72-h in Figure 10.

At 24-h lead-time, the forecast error is modest over the United States and the large errors are mainly concentrated in the area of the stationary low and the related upper level features. Large errors cover a bigger area in the upper troposphere than in the lower troposphere. As the forecast lead time increases, the error at the surface grows locally in the region of the surface low first, and then it slowly expands to the northeast. Errors are larger along the northern than the southern branch of the jet, though rapidly growing in both regions. In the region along the southern branch of the flow the surface pressure errors follow the upper tropospheric errors with a 24-h delay.

## 6.4 Propagation of the forecast improvement

The propagation of the forecast improvement is visualized by a series of *forecast error reduction* figures. This quantity is estimated by

$$100 \times \frac{\sum_{i=1}^{12} \Big( \mid {f_i}^c - {a_i}^c \mid - \mid {f_i}^o - {a_i}^o \mid \Big)}{\sum_{i=1}^{12} \mid {f_i}^c - {a_i}^c \mid}, \tag{9}$$

where ${f_i}^o$ is the operational forecast initiated on the *ith* flight day and ${a_i}^o$ is the verifying analysis from the same analysis cycle. Wherever this quantity is positive the forecast is improved, and wherever it becomes negative the forecast is degraded. The only shortcoming of this verification technique is that large differences between the verifying analyses may obscure changes in the forecast quality at short forecast lead times (see SEA for details).

The forecast error reduction for the surface pressure is shown in Figure 11. The maximum local error reduction in the surface pressure at 24-h lead time exceeds 25% over Alaska and in the region of the stationary surface low. Significant improvements, which are especially large along the southern branch of the jet, start to occur at 48-hour lead time over North America. In the region of the largest forecast errors, along the northern branch of the flow, substantial improvements appear only at 72-h lead time. The presence of these improvements is in contrast with the results of WSR99, when large forecast errors were also found at high latitudes, but those errors were not reduced by the dropsondes.

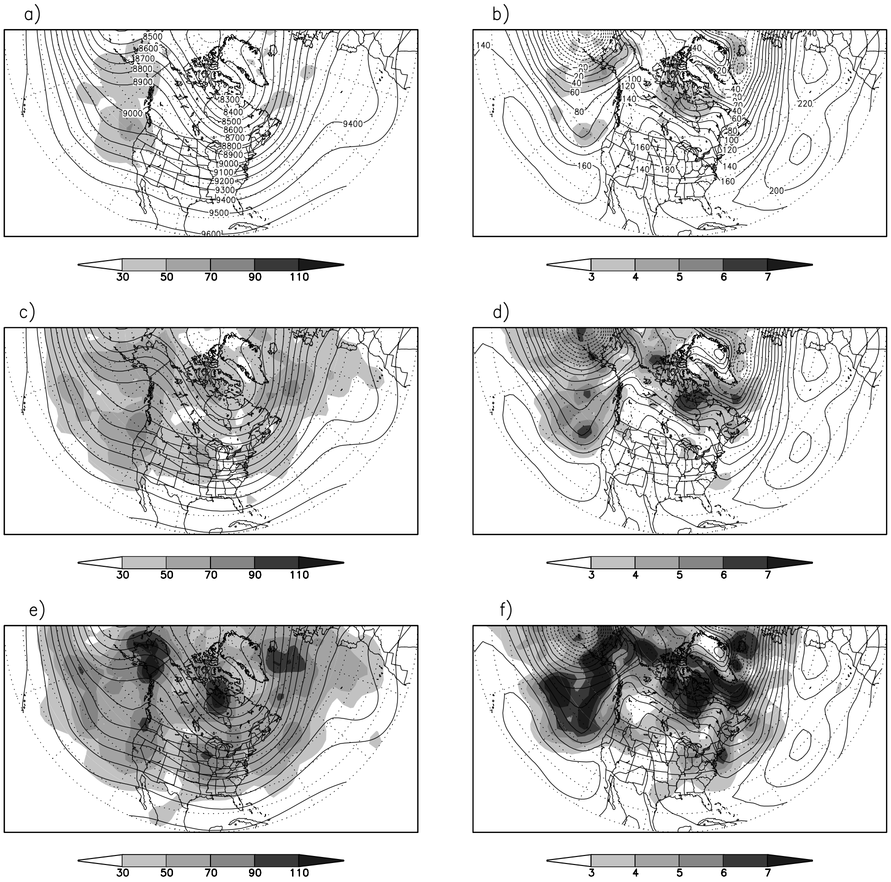

Figure 10: Composite mean of the analysis based estimate of the geopotential height [*gpm*] forecast error (shades) at the 300-hPa pressure level (a, c, e) and for the surface pressure (b, d, f) at 24-, 48-, and 72-h lead times, respectively. Contours show the time-mean of the geopotential height analyses in WSR00 at the 300-hPa (a, c, e) and 1000-hPa (b, d, f) pressure levels.

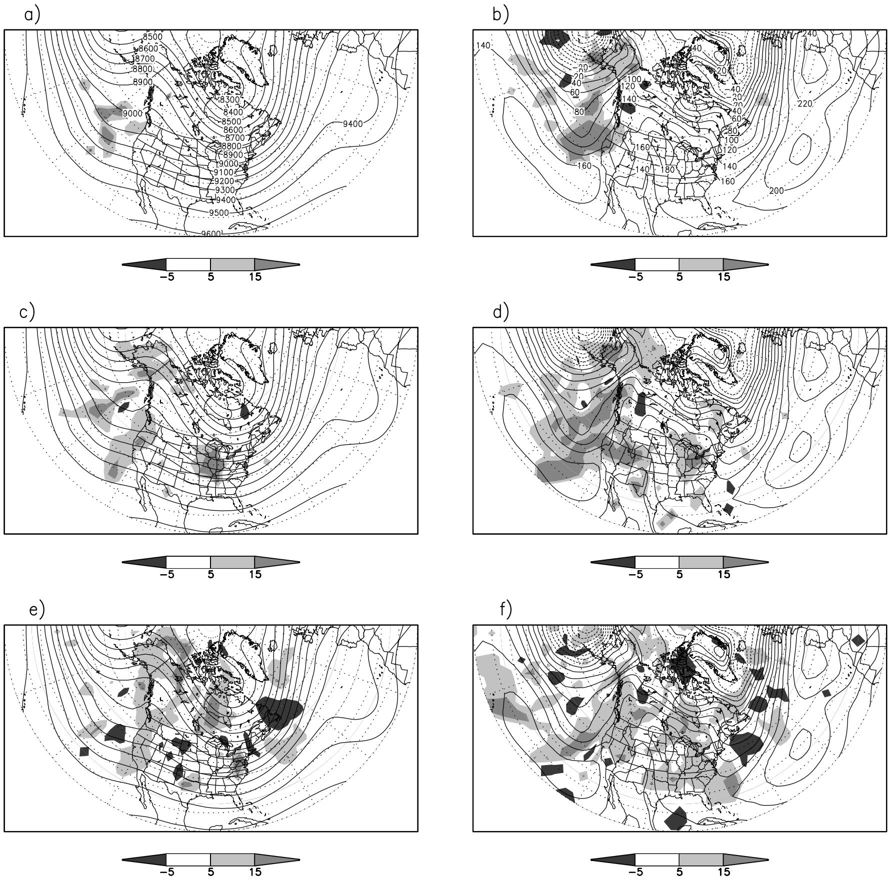

Figure 11: Same as Figure 10, except that shades show forecast error reduction (%) as defined by Equation 9.

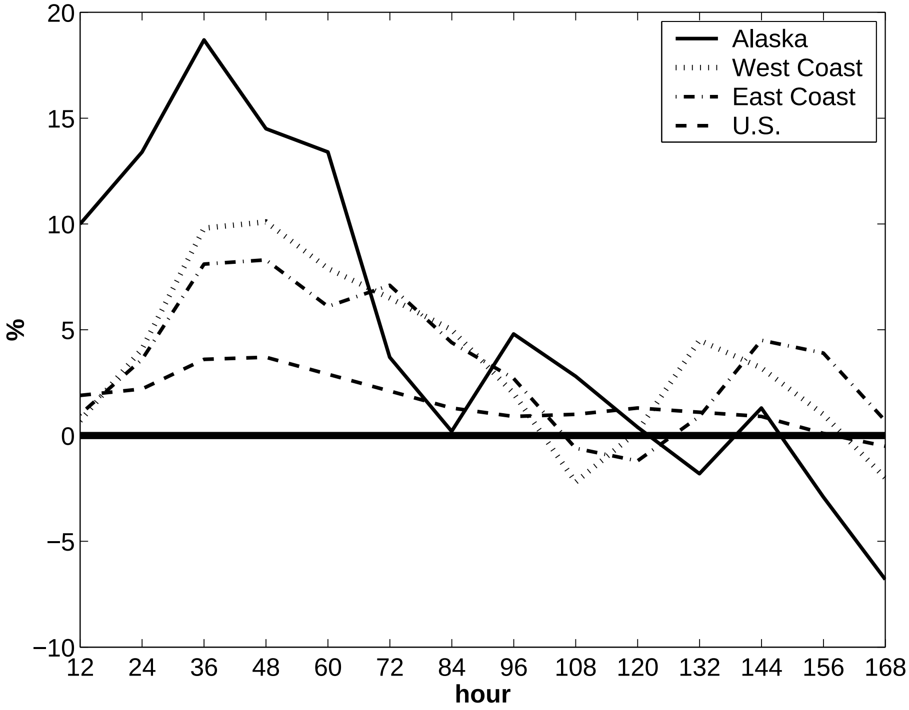

Figure 12: The average surface pressure forecast error reduction for Alaska (165-140W, 55-70N); the west coast (125-100W, 25-50N); the east coast (100-75W); and the the lower 48 states of the United States (125-75W). Positive values show forecast improvement, while negative values show forecast degradation.

The areal average of the forecast error reduction for some selected regions is shown in Figure 12. This figure shows that Alaska benefitted most from the WSR00 program; the forecast error there was reduced by almost 20 % at 36 h forecast time. Over the western half of the United States (called west coast in the figure) the error reduction was about 10 % at 36-48 h lead time. In the latter region the positive influence of the data completely diminishes at around 96 hours, and then returns at 120 hours. This suggests that targeted data improved the forecasts not only along the targeted wave packets, but also along the ones that followed. Over the eastern half of the United States the two peaks of improvement, observed at 72 and 144 hours, followed two peaks of improvement over the western half with a 24 hour delay. This is about the time it takes for a wave packet to travel from the western to the eastern half of the country.

While indisputable error reduction was only observed at the leading edge of the signal during WSR99, long lasting improvements were also observed behind the leading edge in WSR00. The results indicate that this additional improvement was related to the improved prediction of the stationary synoptic features, which played an important role in the propagation of the synoptic waves. This finding is in line with the results of Miguez-Macho and Paegle (2001), who found that analysis uncertainties in the large scale features may play an even more important role in the evolution of errors associated with the prediction of the storms than the initial uncertainties related to the storms themselves.

## 7 Conclusions

Our main findings can be summarized as follows.

- *Targeted data were always collected in regions of important synoptic features*, such as upper tropospheric waves and/or mature surface cyclones. In these targeted regions at least one of the eddy kinetic energy conversion processes had strong local maxima. These processes include the baroclinic energy conversion, the convergence of the ageostrophic geopotential fluxes, and the barotropic energy conversion. The latter played an important role during WSR00 due to the strong deformation of the large scale flow in the northeast Pacific region.
- There were two types of targeting cases in WSR00; in some cases the land-falling system itself was targeted, while at other times the goal was to improve the prediction of storms that formed far downstream from the targeted region. *The data tended to have the largest effect when land-falling synoptic systems were targeted, the baroclinic energy conversion was strong at targeting time, and the convergence of the ageostrophic geopotential fluxes was strong at the verification time.* The latest results confirmed that *downstream baroclinic development plays a major role in propagating the influence of the targeted data.* The results also showed, however, that in the presence of a complex large scale flow, such as was observed during WSR00, controlling the exact downstream location of significant forecast changes can be difficult for longer (4-6-day) lead times.
- The *strong zonal inhomogenities in the large scale flow did not reduce the beneficial forecast effect* of the targeted data. On the contrary, the overall impact of the targeted data on the quality of the forecasts was more positive than before. This can be attributed to the improved prediction of the large scale flow that led to the improved prediction of such characteristics of the synoptic waves as the barotropic energy conversion and the position of the waves. The surface pressure forecast error along the storm track and in the region of stationary features of the flow on average was reduced by 15-25% on average. Of the 23 targeting cases 16 (15) improved and 2 (8) degraded the surface pressure (tropospheric wind) forecasts, while on 5 occasions the surface pressure impact was neutral.

While the present study provides convincing evidence that there is a close relationship between the energetics of the synoptic-scale waves and the propagation of the influence of the targeted data, our results call for further theoretical investigation. Targeting techniques should be tested using simple models and flow configurations, such as those studied in Swanson and Pierrehumbert (1994) and Whitaker and Dole (1995). Experiments with these simple systems could help us understand the potentials and limitations of the currently used linear sensitivity analysis techniques. They could also enhance our understanding of the relationship between the leading edge dynamics and the impact of the targeted data on forecast quality.

The latest results confirm that collecting targeted dropsonde observations over the northeast Pacific is a *practical way of improving severe winter storm forecasts* over the continental United States in the short and the early medium forecast range. Based on the positive experience accumulated during the field programs, the winter storm reconnaissance program has been continued as planned (Toth et al., 2001).

## Acknowledgments

The 2000 Winter Storm Reconnaissance Program, and hence this study, would not have been possible without the work of a large number of participants and collaborators. First, we would like to acknowledge the dedicated work of the NOAA G-lV (led by Sean White) and the USAF Reserve C-130 flight crews (coordinated by Jon Talbot). Coordination with the flight facilities was provided by CARCAH, led by John Pavone. The European Centre for Medium-Range Weather Forecasts is credited for providing their ensemble forecast data in real time for the sensitivity calculations. The forecast cases were selected in real time by NWS field office and NCEP/HPC forecasters coordinated by David Reynolds. Mark Iredell, Jack Woollen and Gyorgyi Gyarmati provided valuable help with setting up the parallel analysis/forecast cycle, manipulating data, and creating graphics. The support and advice of Stephen Lord of EMC in organizing and running the field program was invaluable. Wesley Ebisuzaki, Russ Treadon and two anonymous reviewers provided helpful comments on earlier versions of the paper. The work of I. Szunyogh during the revision of the paper and the work of A. Zimin was supported by the Keck Foundation, while the work of S. J. Majumdar was partly supported by the grants NSF ATM-96-12502 and NSF ATM-98-14376.

# Appendix

### Description of the individual targeting cases

In this Appendix the notions 'strong', 'modest', and 'weak' for the description of the baroclinic energy conversion and the convergence of ageostrophic geopotential fluxes are used according to the definition given in the caption of Table 2. The categories for the barotropic energy conversion term are defined by the same thresholds as for the baroclinic conversion term except that the sign of the conversion can be either positive or negative. When a particular conversion term is not mentioned it means that it played insignificant role for the given case.

*23 January:* The two flights sampled different parts of a splitting upper tropospheric wave packet. One aircraft released sondes over the warm sector of a surface low south of the Aleutians. In this region the baroclinic energy conversion, the convergence of the ageostrophic geopotential fluxes, and the barotropic energy conversion were all strong. The other flight took observations of a wave that was a shallow low at the surface with a well developed trough aloft. The northern sector of the flight was in a region of strong positive, while the southern sector in a region of strong negative barotropic energy conversion. The other energy conversion terms were weak.

*25 January:* Text and figures describing this case are provided in section 5.1.

*26 January:* The single flight sampled a region of strong baroclinic and modest barotropic energy conversion south of the Aleutians.

*28 January:* One flight was a loop from Alaska to the south. It sampled a weak cyclonic wave at the surface and strong westerly/south-westerly flow in the upper troposphere. In the region observed by the flight the eddy kinetic energy was high and the baroclinic energy conversion was modest. Observations taken on the western (eastern) leg of the flight sampled a region of strong negative (positive) barotropic energy conversion. The other flight from Hawaii was a loop to the north-east and observed the region of a weak cyclonic wave. In this area the energy conversion was insignificant.

*30 January:* Both flights, one from Alaska and the other from Hawaii, sampled the same mature cyclone, which was a deep low at the surface and a strong wave in the upper troposphere. At the time the observations were taken the negative barotropic energy conversion was strong, while the other forms of the energy conversion were modest.

*1 February:* On the flight from San Francisco to Honolulu dropsondes were released in the region of an upper level trough and the associated shallow surface low. The barotropic (baroclinic) energy conversion was strong in the eastern (western) sector of the flight. The convergence of the ageostrophic fluxes was also strong in the western sector.

*2 February:* The single flight from Honolulu cut through a deep trough from the side of the cold advection. Some sondes were released in a region of modest energy conversions.

*Note:* The flow, especially the wave packet that reached the northeast Pacific at around 7 February, was favorable for targeting between 2 and 9 February. However, no operable aircraft were available due to mechanical problems during this period.

*9 February:* The single flight from Anchorage sampled a weak cyclonic wave that deepened through baroclinic energy conversion prior to the flight mission. At the time of the flight mission the barotropic energy conversion was strong positive (negative) along the western (eastern) leg of the flight.

*11 February:* The single flight from Honolulu sampled the leading edge of a wave packet associated with a weak closed low that developed in the warm sector of a deep large scale cyclone. There was weak baroclinic energy conversion at observational time.

*13 February:* This flight sampled the trailing edge of the same upper tropospheric wave packet that was sampled by the flight on 11 January. The baroclinic energy conversion was modest in the area targeted by the observations.

*14 February:* A weak cyclonic wave, left behind by the wave packet already targeted twice, was sampled on a flight from Honolulu. There was modest baroclinic energy conversion in the observed region.

*16 February:* The targeted data were taken during a ferry flight. Three of the sondes sampled the southern edge of a system that was a closed low both at the surface and the 300-hPa level and where both energy conversion terms were weak.

# References

Bergot, T., G. Hello, and A. Joly, 1999: Adaptive observations: indent a feasibility study. *Mon. Wea. Rev.,* **127,** 743-765.

Bishop, C. H., 1993a: On the behavior of baroclinic waves undergoing horizontal deformation. I: The 'RT' phase diagram. *Q. J. Roy. Meteorol. Soc.,* **119,** 221-240.

Bishop, C. H., 1993b: On the behavior of baroclinic waves undergoing horizontal deformation. II: Error-bound amplification and Rossby wave diagnostics. *Q. J. Roy. Meteorol. Soc.,* **119,** 241-267.

Bishop, C. H. and Z. Toth, 1999: Ensemble transformation and adaptive observations. *J. Atmos. Sci.,* **56,** 1748-1765.

Bishop, C. H., B. J. Etherton, and S. J. Majumdar, 2001: Adaptive sampling with the Ensemble Transform Kalman Filter Part I: Theoretical aspects. *Mon.*

*Wea. Rev.,* **129,** 420-436.

Bloomfield, 1976: *Fourier Analysis of Time Series: An Introduction.* Wiley-Interscience, 258 pp.

Buizza, R., T. Petroliagis, T. N. Palmer, J. Barkmeijer, M. Hamrud, A. Hollingsworth, A. Simmons, and N. Weidi, 1998: Impact of model resolution and ensemble size on the performance of an ensemble prediction system. *Q. J. Roy. Meteorol. Soc.,* **124,** 1935-1960.

Buizza, R. and Montani, A., 1999: Targeting observations using singular vectors. *J. Atmos. Sci.,* **56,** 2965-2985.

Chang, E. K. M. and I. Orlanski, 1993: On the dynamics of storm tracks. *J. Atmos. Sci.,* **50,** 999-1015.

Chang, E. K. M., 1999: Wave packets and life cycles of troughs in the upper troposhere: Examples from the Southern Hemisphere Summer Season of 1984/85. *Mon. Wea. Rev.,* **126,** 25-50.

Chang, E. K. M. and D. B. Yu, 1999: Characteristics of wave packets in the upper troposphere. Part I: Northern Hemisphere Winter. *J. Atmos. Sci.,* **56,** 1708-1728.

Charney, J. G., 1949: On a physical basis for numerical prediction of large-scale motions in the atmosphere. *J. Meteor..,* , **6,** 371-385.

Errico, R., T. Vukicevic, and K. Reader, 1993: Comparison of initial and lateral boundary condition sensitivity for a limited-area model. *Tellus,* **45,** 539-577.

Ertel, H., 1941: Die Unmöglichkeit einer exacten Wetterprognose auf Grund synoptischer Luftdruckkarten von Teilgebieten der Erde. *Meteor. Z.,* **58,** 309-313.

Ertel, H., 1944: Wettervorhersage als Randwertproblem. *Meteor. Z.,* **61,** 181-190.

Emanuel, K. A, E. N. Lorenz, and R. E. Morss, 1996: Adaptive observations. *Preprints of the 11th AMS Conference on Numerical Weather Prediction,* August, 19-23, 1996, Norfolk, VA, 67-69.

Gelaro, R., R. H. Langland, G. D. Rohaly, T. E. Rossmond, 1999: An assessment of the singular-vector approach to target observations using the FASTEX dataset. Quart, J. Roy. Meteor. Soc., 125, 3299-3328.

Hartmann, D. L., R. Buizza, and T. N. Palmer, 1995: Singular vectors: The effect of spatial scales on linear growth of disturbances. *J. Atmos. Sci.,* **52,** 3885-3894.

Hoskins, B. J., R. Buizza and J. Badger, 2000: The nature of singular vector growth and structure. *Q. J. Roy. Meteorol. Soc.,* **126,** 1565-1580.

Hovmöller, E., 1949: The trough-and-ridge diagram. *Tellus,* **1,** 62-66.

Langland, R. H., Z. Toth, R. Gelaro, I. Szunyogh, M. A. Shapiro, S. Majumdar, R. Morss, G. D. Rohaly, C. Velden, N. Bond, and C. Bishop, 1999: The North-Pacific Experiment (NORPEX-98) Targeted observations for improved North American Weather Forecasts. *Bull. Amer. Meteorol. Soc.,* **80,** 1363-1384.

Langland, R. H., and G. D. Rohaly, 1996: Analysis error and adjoint sensitivity in the prediction of a North-Atlantic frontal cyclone. *Proc. 11th Conference on Numerical Weather Prediction,* Norfolk, VA, Amer. Meteor. Soc., 150-152.

Lorenz, E. N., and K. A. Emanuel, 1998: Optimal sites for supplementary weather observations: simulations with a small model. *J. Atmos. Sci.,* **55,** 633-653.

Majumdar, S. J., C. H. Bishop, B. J. Etherton, Z. Toth, 2001a: Adaptive sampling with the Ensemble Transform Kalman Filter. Part II: Field program implementation. *Mon. Wea. Rev.,* (under review).

Majumdar, S. J., C. H. Bishop, I. Szunyogh, and Z. Toth, 20001b: Can an Ensemble Transform Kalman Filter predict reduction in forecast error variance produced by targeted observations? *Q. J. Roy. Meteorol. Soc.,* (in press).

Miguez-Macho, G., and J. Paegle, 2001: Sensitivity of North American numerical weather prediction to initial state uncertainty in selected upstream subdomains. *Mon. Wea. Rev.,* **129,** 2005-2022.

Montani, A., A. J. Thorpe, R. Buizza, and P. Unden, 1999: Forecast skill of the ECMWF model using targeted observations during FASTEX. *Q. J. Roy. Meteorol. Soc.,* **125,** 3219-3240.

Morss, R. E., and K. A. Emanuel, 2000a: Influence of added observations on analysis and forecast errors. *Q. J. Roy. Meteorol. Soc.,* (in press).

Morss, R. E., K. A. Emanuel, and C. Snyder, 2000b: Idealized adaptive observation strategies for improving numerical weather prediction. *J. Atmos. Sci.* **58,** 210-232.

Orlanski, I., and J. Katzfey, 1991: The life cycle of a cyclone wave in the Southern Hemisphere. Part I: Eddy energy budget. *J. Atmos. Sci.,* **48,** 1972-1998.

Orlanski, I. and J. P. Sheldon, 1993: A case of downstream baroclinic development over wester North America. *Mon. Wea. Rev.,* **121,** 2929-2950.

Palmer, T. N., R. Gelaro, J. Barkmeijer, and R. Buizza, 1998: Singular vectors, metrics, and adaptive observations. *J. Atmos. Sci.,* **55,** 633-653.

Parrish, D. F., and J. C. Derber, 1992: The National Meteorological Center's Spectral Statistical-Interpolation Analysis System. *Mon. Wea. Rev.,* **120,** 1747-1763.

Parrish, D. F., J. C. Derber, R. J. Purser, W.-S. Wu, and Z.-X. Pu, 1997: The NCEP global analysis system: Recent improvements and future plans. *J. Met. Soc. Japan,* **75, 1B,** 359-365.

Pedlosky, J., 1987: *Geophysical fluid dynamics.* Second Ed., Springer-Verlag, pp. 710.

Persson, A., 2000: Synoptic-dynamic diagnosis of medium range weather forecast systems. *Proceedings of the Seminars on Diagnosis of models and data assimilation systems.* 6-10 September 1999, ECMWF, Reading, U.K., 123-137.

Phillips, N. A., 1976: The impact of synoptic observing and analysis systems on flow pattern forecasts. *Bull. Amer. Meteorol. Soc.,* **43,** 1225-1240.

Phillips, N. A., 1990: *Dispersion processes in large-scale weather prediction.* WMO-No. 700, World Meteorological Organization, pp. 126.

Pu, Z.-X., S. Lord, and E. Kalnay, 1998: Forecast sensitivity with dropwindsonde data and targeted observations. *Tellus,* **50A,** 391.

Pu, Z.-X., and E. Kalnay, 1999: Targeting observations with the quasi-inverse linear and adjoint NCEP global models: Performance during FASTEX. *Q. J. Roy. Meteorol. Soc.,* **125,** 3329-3337.

Rabier, F., P. Courtier, and O. Talagrand, 1992: An application of adjoint models to sensitivity analysis. *Beitr. Phys. Atmos.,* **65,** 177-192.

Rabier, F., E. Klinker, P. Courtier, and A. Hollingsworth, 1996: Sensitivity of forecast errors to initial conditions. *Quart. J. Roy. Meteorol. Soc.,* **122,** 121-150.

Rossby, C.-G., 1945: On the propagation of frequencies and energy in certain types of oceanic and atmospheric waves. *J. Meteor.,* **2,** 187-204.

Rossby, C.-G., 1949: On the dispersion of planetary waves in a barotropic atmosphere. *Tellus,* **1,** 54-58.

Snyder, C., 1996: Summary of an informal workshop on adaptive observations and FASTEX. *Bull. Am. Meteorol. Soc.,* **77,** 953-961.

Swanson, K., and R. T. Pierrehumbert, 1994: Nonlinear Wave packet evolution on a baroclinically unstable jet. *J. Atmos. Sci.,* **51,** 384-396.

Szunyogh, I., E. Kalnay, and Z. Toth, 1997: A comparison of Lyapunov and optimal vectors in a low-resolution GCM. *Tellus,* **49A,** 200-227.

Szunyogh, I., Z. Toth, K. A. Emanuel, C. H. Bishop, C. Snyder, R. E. Morss, J. Woolen, and T. Marchok, 1999a: Ensemble-based targeting experiments during FASTEX: the effect of dropsonde data from the Lear jet. *Quart. J. Roy. Meteor. Soc.*, **125,**, 3189-3218.

Szunyogh, I., Z. Toth, S. J. Majumdar, R. E. Morss, C. H. Bishop and S. Lord, 1999b: Ensemble-based targeted observations during NORPEX. *Third Symposium on Integrating Observing Systems,* January, 10-15, 1999, Dallas, TX, AMS, 74-77.

Szunyogh, I., Z. Toth, R. E. Morss, S. J. Majumdar, B. J. Etherton, and C. H. Bishop, 2000: The effect of targeted dropsonde observations during the 1999 Winter Storm Reconnaissance Program. *Mon. Wea. Rev.,* **128,** 3520-3537.

Toth, Z., and Kalnay, E., 1993: Ensemble forecasting at NMC: The generation of perturbations. *Bull. Amer. Meteorol. Soc.,* **74,** 2317-2330.

Toth, Z., and E. Kalnay, 1997: Ensemble forecasting at NCEP and the breeding method. *Mon. Wea. Rev.*, **125,** 3297-3319.

Toth, Z., E. Kalnay, S. M. Tracton, R. Wobus, and J. Irwin, 1997: A synoptic evaluation of the NCEP ensemble. *Wea. Forecasting,* **12,** 140-153.

Toth, Z., I. Szunyogh, S. J. Majumdar, R. E. Morss, B. J. Etherton, C. H. Bishop, S. J. Lord, M. Ralph, O. Persson and Z.-X. Pu, 2000: Targeted observations at NCEP: Toward an operational implementation. *Fourth Symposium on Integrating Observing Systems,* January, 10-14, 2000, Long Beach, CA, AMS, 186-193.

Toth, Z., I. Szunyogh, C. Bishop, S. Majumdar, R. Morss, and S. Lord, 2001: On the use of targeted observations in operational weather prediction. *Fifth Symposium on Integrating Observing Systems,* January 15-19 2000, Albuquerque, NM, AMS (in print).

Yeh, T., 1949: On energy dispersion in the atmosphere. *J. Meteor.,* **6,** 1-16.

Whitaker, J. S., and R. M. Dole, 1995: Organization of storm tracks in zonally varying flows. **52,** 1178-1191.